RSC Advances

PAPER

View Article Online
View Journal | View Issue

Cite this: *RSC Adv.*, 2026, **16**, 9991

Imidazole-2-thiohydantoin conjugates for trace water detection in organic solvents and visual colour recognition for real-time monitoring

Bhagwat Giri Goswami,[ab] Amutha Selvaganesan,[a] Kommineni Kalyani,[c] K. K. R. Datta *[a] and Venkatramaiah Nutalapati *[ad]

Trace water is a detrimental impurity present in organic solvents that negatively impacts various organic reactions, necessitating the development of new sensitive and selective methods for its detection. In this study, we develop two novel donor–acceptor molecules, **Im-2TH** and **Di-OMeIm-2TH**, using a Knoevenagel condensation reaction between imidazole-based aldehydes and 2-thiohydantoin. **Im-2TH** and **Di-OMeIm-2TH** show intramolecular charge transfer (ICT) bands at 414 and 425 nm, along with strong green and yellow emissions at 550 and 585 nm in THF, respectively. Both compounds exhibit strong solvatochromic behaviour with changes in the polarity of the solvent and show aggregation-induced emission (AIE) characteristics with distinct variations in their surface morphology (spheres, fibers, and needle-shaped flakes) as the fraction of water varies in THF, ACN and DMSO mixtures. Consequently, tuning their surface morphology and change in their emission behaviour offer potential for trace water detection in organic solvents. **Di-OMeIm-2TH** exhibits superior sensitivity compared with **Im-2TH**, as evident from its higher K_{sv} values of 1.3945, 3.117, and 0.6787 M^{-1} with limit of detection (LOD) of 0.060, 0.034 and 0.124 ppm in THF, ACN, and DMSO, respectively. Furthermore, **Im-2TH** and **Di-OMeIm-2TH** were employed for trace water detection in real samples such as cement, sand, sugar, salt and detergent powder. A smart phone-based fluorometric assay is developed for the recognition of colour variation and RGB array profiles to facilitate the detection of water content in organic solvents for real-time monitoring.

Received 15th December 2025
Accepted 3rd February 2026

DOI: 10.1039/d5ra09696k

rsc.li/rsc-advances

1 Introduction

Trace levels of water present as solvent impurities readily react with highly reactive organometallic intermediates, leading to their quenching. This deactivation adversely affects moisture-sensitive transformations such as the Grignard, Wittig, and Friedel–Crafts reactions, resulting in diminished yields, poor selectivity, and altered reaction kinetics.[1,2] Active metals such as sodium and potassium (in pure form) are preserved in hydrocarbon solvents to avoid trace water impurities that cause damage to the metal, which can lead to accidents *via* explosion owing to the generation of hydrogen gas ($2Na + 2H_2O \rightarrow 2NaOH + H_2\uparrow$).[3] Hence, the use of anhydrous solvents is critical while performing water-sensitive reactions. Similarly, trace levels of water impurities in pharmaceuticals can adversely affect their physiological stability and therapeutic efficacy.[4] Furthermore, in petroleum plants, trace water contamination in fuels can result in reduced engine power and efficiency. Particularly, at lower temperatures, emulsification and phase separation might occur, leading to clogged fuel ducts and ultimately engine damage.[5] Thus, the qualitative and quantitative detection of trace water in reaction mixtures is imperative. Conventional techniques such as Karl-Fischer (KF) titration, electrochemical methods and chromatographic methods are used to detect trace water. KF titration is widely used for ppm-level water detection, but it suffers from drawbacks such as multistep sample preparation and the use of sensitive reagents (CH_3OH, I_2, and SO_2).[6] Electronic sensors for moisture detection are commercially available in the market but suffer from limitations such as high cost, limited lifetime, operational errors and require continuous monitoring by technical experts.[7] Therefore, the development of alternative methods that are simpler and more sensitive for the detection of trace water is critically required. To overcome these challenges, fluorescence-based sensors are attractive due to their high selectivity, sensitivity, low cost, and ease of handling.[8] Notably, donor–acceptor systems with an

[a]*Department of Chemistry, Faculty of Engineering and Technology, SRM Institute of Science and Technology, SRM Nagar, Kattankulathur, 603203, India. E-mail: kumarard@srmist.edu.in*

[b]*Department of Chemistry, SSSTSRGDC, Nainidanda Pauri, Garhwal 246277, Uttarakhand, India*

[c]*Department of Chemistry, RVR&JC College of Engineering, Guntur, Andhra Pradesh 522019, India*

[d]*Centre for Interdisciplinary Research (CIDR), SRM University-AP, Amaravati, Andhra Pradesh 522 240, India. E-mail: nvenkat83@gmail.com; venkatramaiah.n@srmap.edu.in*

olefinic core exhibit excited-state intramolecular charge transfer and are highly sensitive to solvent polarity. Based on this strategy, numerous fluorescent probes have been reported for trace water detection, incorporating various fluorophore units such as 1,8-naphthalimide,[9] thioxanthone,[10] 8-hydroxyquinoline,[11] and fluoranthene.[12] Das *et al.* reported on a quinoxaline-based fluorescent probe, 6*H*-indolo[2,3-*b*]quinoxalin-3-amine (L1), which can detect moisture in different solvents such as acetonitrile, THF, DMF, and MeOH with a limit of detection (LOD) of 0.018%, 0.027%, 0.012%, and 0.43%, respectively.[13] Zeng *et al.* developed the triphenylamine-based conjugated compounds TPA-TSC and di-TPA-TSC, where the triphenylamine unit acts as a donor and the thiosemicarbazone group acts as an acceptor, which can detect moisture in organic solvents and effectively work in acetonitrile with LODs of 0.0079 vol% and 0.0071 vol%, respectively.[14] Xie *et al.* reported on sulphur and nitrogen co-doped carbon dots (O-CDs), which showed solvatochromism in the solution phase and can detect trace water in organic solvents, particularly in acetone, with an LOD of 0.042%.[15] However, most of the reports in the literature involve tedious synthesis, low sensitivity, and high LODs. Imidazole-based probes have recently gained significant attention due to their unique properties, such as straightforward synthesis and ease of structural modification to fine-tune their fluorescence behaviour for deep-blue OLEDs with high thermal stability,[16,17] chemo-sensors for anti-counterfeiting[18] and various biologically active analytes.[19] Iyer *et al.* synthesized a diphenylimidazole-based fluorescent probe, Im-2ATP, having 2-aminothiophenol as a recognition unit. Im-2ATP shows a selective turn-ON response with Hg^{2+} and Cr^{3+} in a semi-aqueous medium of CH_3CN–H_2O (8 : 2, v/v) with an LOD of 6 nM and 1.96 nM, respectively.[20] Wang *et al.* developed a diphenylimidazole-based probe, DIP, for sensing fluoride ions and trace water with an LOD of 72.3 nM and 0.0015 vol%, respectively. DIP involved a deprotonation–protonation strategy to detect F^- ions and trace water.[21] Nagabhushana *et al.* developed an AIE-based imidazole derivative, FDIP, and employed it for the fluorescence visualization of latent finger prints (LFPs).[22] 2-Thiohydantoin (2TH) is a sulphur analogue of the non-aromatic five-membered heterocyclic hydantoin containing thiocarbonyl and carbonyl groups at the C_2 and C_4 positions with two nitrogen atoms at the C_1 and C_3 positions, respectively. 2TH acts as an acceptor as well as a metal ion chelator due to the presence of –C=O and –C=S bonds and heteroatoms such as N, S, and O.[23–25] Recently, our research group reported on 2-thiohydantoin-based five different donor–acceptor systems developed by C_5 substitution on 2TH. Among all, *N*,*N*-diMeAPh-2TH exhibits selective vapochromism towards nonanal vapour, resulting in a colour transition from orange to brown. *N*,*N*-diMeAPh-2TH shows p-type behavior for nonanal vapours with a high surface photovoltage (SPV) response of 94% within 293 s and recovery (87%) in surface PVT in 692 s.[26]

In continuation of our efforts in the design and development of novel fluorescent probes for the detection of various anthropogenic ions with visual colour recognition behaviour,[27–30] we engineered and synthesized two fluorescent probes with varying substituents, **Im-2TH** and **Di-OMeIm-2TH**, using a one-pot Knoevenagel condensation reaction between Im-CHO/Di-OMeIm-CHO and 2-thiohydantoin. **Im-2TH** and **Di-OMeIm-2TH** show exceptional solvatochromic behavior and high sensitivity towards trace water in organic solvents such as tetrahydrofuran (THF), acetonitrile (ACN), and dimethyl sulfoxide (DMSO) with ratiometric fluorescence response behavior. **Di-OMeIm-2TH** shows higher sensitivity towards trace water impurities (34–124 ppb) due to the presence of two –OMe groups, which amplify the donor strength of the diphenylimidazole core *via* improved intramolecular charge transfer (ICT) properties. **Im-2TH** and **Di-OMeIm-2TH** form different nanoscale structures, such as nanospheres, nanofibers, needle nanoflakes, nanoflakes, and branched nanoflakes, with a variation in the polarity of the medium. Both **Im-2TH** and **Di-OMeIm-2TH** exhibit aggregation-induced emission (AIE) behavior and show light green and light orange colour emission at $f_w = 80\%$. Further, both probes were utilized to detect trace water impurities in real samples of raw building materials such as cement, sand, and detergent powder, besides food products such as salt and sugar. A smartphone-assisted RGB colour recognition assay was developed to detect the water content in different organic solvents, which is beneficial for the real-time monitoring of trace water with naked eye fluorescence and lipid droplet imaging.

2 Experimental section

2.1 Materials and method

All chemicals and solvents of HPLC grade were purchased from Sigma-Aldrich and Avra, India. Double-distilled water obtained from MilliQ system (<18.2 MΩ) was used for sample preparation. Fourier-transform infrared (FT-IR) spectra were recorded on a Shimadzu IRTracer-100 using ATR mode. ^1H $\{^{13}C\}$ NMR spectra were recorded on a Bruker 500{125} MHz spectrometer using tetramethylsilane (TMS) as the internal reference. High-resolution mass spectrometry (HR-MS) was performed using a 6230B time-of-flight (TOF) system, Agilent Technologies. Absorption spectra were recorded on an Agilent Cary 60 UV-visible spectrophotometer. Fluorescence spectra were obtained using an Edinburgh FLS 1000 spectrofluorometer. Time-resolved fluorescence emission decay spectra were obtained using the time-correlated single photon counting (TCSPC) technique using a 450 nm LED (ns). Absolute quantum yields were measured through an integrated sphere system. High-resolution scanning electron microscopy (HR-SEM) images were obtained using a Thermo Fisher Scientific Apreo S Hi-Resolution Scanning Electron Microscope. HOMO and LUMO energies and the corresponding energy gaps were calculated using first-principles DFT implemented in the Gaussian16 software with the 6-311G+(d, p) basis set and B3LYP hybrid functional.

2.2 Real sample preparation

Raw building materials, including cement and sand, were collected from the Architecture Department of SRMIST. Food samples were collected from a local market near SRMIST. We added 30 mg of each as raw material to a solution of **Im-2TH**

and **Di-OMeIm-2TH** (10 μM in dry THF). After centrifuging at 9000 rpm for 10 min, the mixture was filtered to obtain a clear solution and directly used for analysis. For dry samples, all the raw materials were oven-dried overnight.[13]

2.3 RGB assay analysis

2 mL of **Im-2TH** and **Di-OMeIm-2TH** (10 μM) in different solvents was added to a 5 mL neat and clean glass vial. Different fractions of water (0–6% v/v) were gradually added to this solution, and the changes in the colour of the solution under light exposure at 365 nm were monitored. RGB analysis was carried out using the RGB colour application with a smartphone (model SM-A146B/DS) having a camera of 50 MP + 2 MP + 2 MP + 2 MP. The distance between the sample and the light source was kept constant at ~15 cm. Similarly, the distance between the smartphone camera and the sample vial was kept constant at 30 cm.

2.4 Synthesis of (*Z*)-5-(4-(4,5-diphenyl-1*H*-imidazole-2-yl) benzylidene)-2-thioxoimidazolidin-4-one (Im-2TH)

In a 25 mL round-bottom flask, 2-thiohydantoin (106 mg, 1 mmol) and sodium acetate (301 mg, 4 mmol) were added to 10 mL glacial acetic acid. The reaction mixture was stirred for 30 min, and then 4-(5-(cyclohexa-2,4-dien-1-yl)-4-phenyl-1*H*-imidazole-2-yl)benzaldehyde (300 mg, 1 mmol) was added, and the reaction was kept under reflux for 12 h. The reaction progress was monitored by using thin-layer chromatography (TLC). After completion of the reaction, the mixture was poured into ice-cold water, resulting in the formation of a dark orange precipitate, which was subsequently filtered to obtain the crude product. The crude product was further purified by column chromatography using hexane-chloroform (50 : 50 v/v), and a dark orange-coloured product was obtained in 84% yield (330 mg). ^{1}H NMR (500 MHz, DMSO-d_6) (ppm): δ 12.83 (s, 1H), 12.30 (s, 2H), 8.14–8.11 (d, 2H, J = 15 Hz), 7.89–7.86 (d, 2H, J = 15 Hz), 7.57–7.21 (m, 10H), 6.51 (s, 1H). ^{13}C NMR (125 MHz): 179.63 (–C=S), 172.50 (–C=O), 166.43 (N–C=N), 144.56 (2TH-carbon), 138.15–125.30 (aromatic carbon), 111.46 (ethylene carbon). Calculated mass of $C_{25}H_{18}N_4OS$: 422.1201 found: 423.1261 $[M + H]^+$.

2.4.1 (*Z*)-5-(4-(4,5-Bis(4-methoxyphenyl)-1*H*-imidazole-2-yl) benzylidene)-2-thioxoimidazolidin-4-one (Di-OMeIm-2TH).

Under a similar experimental conditions of **Im-2TH**, the compound **Di-OMeIm-2TH** was prepared using 4-(4,5-bis(4-methoxyphenyl)-1*H*-imidazole-2-yl)benzaldehyde (301 mg, 1 mmol) as the precursor. The reaction progress was monitored using thin-layer chromatography (TLC). After the reaction was complete, the mixture was poured into ice-cold water, resulting in the formation of a dark orange precipitate, which was subsequently filtered to obtain the crude product. The crude product was further purified by column chromatography using chloroform, and a dark orange-red coloured product was obtained in 67% yield (300 mg). ^{1}H NMR (500 MHz, DMSO-d_6) (ppm): δ 12.44 (s, 1H), 12.24 (s, 1H), 8.12–8.10 (d, 2H 10 Hz), 7.87–7.85 (d, 2H, 10 Hz), 7.47–7.45 (d, 5H, 10 Hz), 6.96–6.97 (d, 5H, 5 MHz), 6.52 (s, 1H), 3.78 (s, 6H). ^{13}C NMR (125 MHz): 179.51 (–C=S), 172.52 (–C=O), 166.28 (N–C=N), 158.97 (aromatic C–O), 144.56 (2TH carbon), 132.3–114.38 (aromatic carbon), 111.68 (ethylene carbon), 55.59 (O–CH_3). Calculated mass $C_{27}H_{22}N_4O_3S$-482.1413. Found-481.2898 $[M - H]^+$.

3 Result and discussion

In the first step, Im-CHO and Di-OMeIm-CHO were synthesized using the method reported in the literature.[31] Further, **Im-2TH** and **Di-OMeIm-2TH** were synthesized using the Knoevenagel condensation reaction among Im-CHO, Di-OMeIm-CHO, and 2TH under acidic conditions, as outlined in Scheme 1.

Further, the synthesized compounds were characterized using different spectroscopic techniques such as ^{1}H{^{13}C} NMR, FTIR, and HRMS. The ^{1}H NMR spectrum of **Im-2TH** shows an imidazole proton at δ 12.83 ppm, two N–H protons of the thiohydantoin unit at δ 12.30 ppm, aromatic protons at δ 8.14–7.21 ppm, and an ethylenic proton at δ 6.51 ppm (Fig. S1, SI). In the ^{13}C NMR spectrum of **Im-2TH**, –C=S, C=O, and C=N

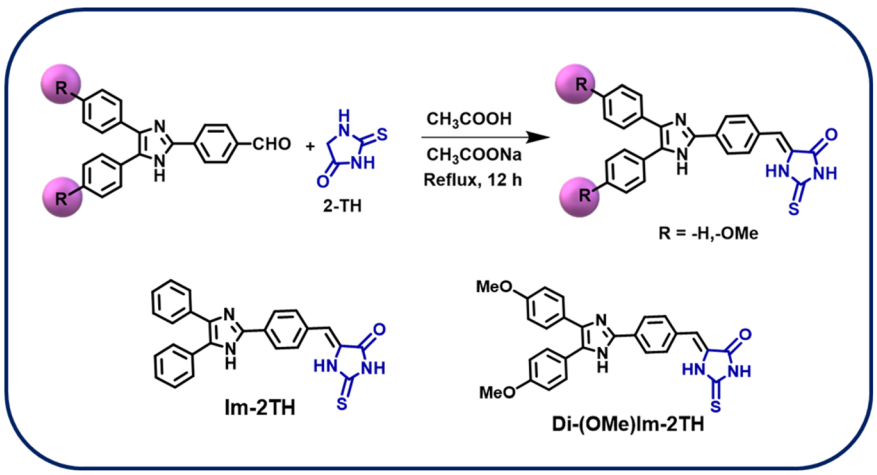

Scheme 1 Synthetic scheme of Im-2TH and Di-OMeIm-2TH.

appear at δ 179.63, 172.50, and 166.43 ppm, respectively. 2-Thiohydantoin carbon appears at δ 144.56 ppm and the ethylenic carbon appears at δ 111.46 ppm (Fig. S2, SI). The ^{1}H NMR spectrum of **Di-OMeIm-2TH** show two N–H protons of the thiohydantoin unit appear at δ 12.44 ppm and δ 12.24 ppm. Due to the presence of two methoxy (–OMe) groups on the phenyl ring, the aromatic protons are slightly shielded and appear at δ 8.12–6.96 ppm. The ethylenic proton appears at δ 6.52 ppm and 6 methyl protons at δ 3.78 ppm (Fig. S3, SI). In the ^{13}C NMR spectrum of **Di-OMeIm-2TH**, –C=S, C=O, and C=N appear at δ 179.51, 172.52, and 166.28 ppm, respectively. 2-Thiohydantoin carbon appears at δ 144.56 ppm, the ethylenic carbon appears at δ 111.68 ppm, and the methyl carbon ($-OCH_3$) appears at δ 55.59 ppm (Fig. S4, SI). The FTIR spectrum of **Im-2TH** shows vibrational bands at 1721 cm^{-1} and 1645 cm^{-1}, corresponding to the –C=O and –C=S functional groups, respectively. The vibrational band located at 3360 cm^{-1} arises due to the N–H proton of thiohydantoin and imidazole. **Di-OMeIm-2TH** shows vibrational bands at 1724 cm^{-1}, 1643 cm^{-1}, and 3367 cm^{-1}, corresponding to the –C=O, –C=S, and N–H protons of the thiohydantoin and imidazole functional groups, respectively (Fig. S5, SI). The $[M + H]^+$ ion peak at 423.1261 and the $[M - H]^+$ ion peak at 481.2898 in the HRMS spectra confirmed the formation of **Im-2TH** and **Di-OMeIm-2TH** (Fig. S6 and S7, SI), respectively. Fig. S8, SI shows the TGA profile with a major weight loss of 33.42% and 40.99% at 300 °C for **Im-2TH** and **Di-OMeIm-2TH**, respectively, due to the decomposition of 2TH.

The photophysical properties of **Im-2TH** and **Di-OMeIm-2TH** were studied in solution and thin films by coating them on a quartz surface using a spin coater. The absorption spectrum of **Im-2TH** in THF shows two absorption bands at 244 nm and 291 nm due to the $\pi \rightarrow \pi^*$ and $n \rightarrow \pi^*$ transitions, respectively. Another strong absorption band is observed at 414 nm due to the ICT process. In thin-film state, **Im-2TH** displays absorption bands at 295 and 424 nm, which are red-shifted by ~4 and ~10 nm, respectively. Similarly, **Di-OMeIm-2TH** exhibits $\pi \rightarrow \pi^*$ and $n \rightarrow \pi^*$ transitions at 252 and 285 nm, respectively, and ICT band at 425 nm in solution, which shifts to 435 nm in the thin film (Fig. 1(a)). **Im-2TH** exhibits a strong bluish-green emission at 550 nm in THF with a quantum yield (Φ) of 63%, whereas **Di-OMeIm-2TH** shows yellow emission at ~585 nm with a higher Φ of 74%. In the thin-film state, **Im-2TH** and **Di-OMeIm-2TH** display red-shifted emissions at 612 nm (~62 nm shift) and 680 nm (~95 nm shift), respectively, indicating the formation of J-type aggregates in the solid state (Fig. 1(b)).

The excitation-dependent emission studies (350–500 nm) reveal an ~3-fold enhancement in the emission intensity of **Im-2TH** upon increasing the excitation wavelength to 420 nm, followed by quenching at higher wavelengths; a similar trend with ~2-fold enhancement at 430 nm is observed for **Di-OMeIm-2TH** (Fig. S9c, SI). Time-resolved fluorescence measurements show a bi-exponential decay for **Im-2TH** with an average lifetime of ~1.44 ns, while **Di-OMeIm-2TH** exhibits a slightly longer average lifetime, which is attributed to the differences in their substitution (Fig. S9b and d, SI), respectively. To investigate the aggregation behaviour of the probes, the concentration-dependent UV-vis spectra of **Im-2TH** and **Di-OMeIm-2TH** were recorded. The absorbance at 244, 291, and 414 nm increased linearly with concentration, following Beer–Lambert's law, indicating the absence of aggregate formation even at higher concentrations (20 μM), while intramolecular charge-transfer (ICT) dominates at lower concentrations (Fig. S9e–h, SI). Similarly, their concentration-dependent emission spectra upon excitation at 414 and 425 nm show a linear increase in emission intensity with concentration, with no significant change in emission maxima or pattern, confirming their negligible aggregation in solution (Fig. S9i–l, SI). To confirm the intramolecular charge-transfer (ICT) mechanism in the donor–acceptor (D–A) architecture, solvatochromic studies were conducted. The absorption spectra of **Im-2TH** and **Di-OMeIm-2TH** show negligible changes with solvent polarity (Fig. S10a and b, SI), whereas their emission spectra exhibit pronounced shifts, reflecting the sensitivity of the excited-state ICT process to the solvent environment (Fig. S10c and d, SI).

In polar solvents such as MeOH, **Im-2TH** shows an emission band at 670 nm, with a red shift of 120 nm, while in non-polar solvents such as hexane, emission bands appear at 495 nm with a blue shift of ~55 nm. In comparison with **Im-2TH**, we have observed a red shift of ~30 nm for **Di-OMeIm-2TH** in methanol, while in nonpolar solvents like hexane, it shows emission with a red shift of ~26 nm (Fig. 2(a) and (b)), respectively. The variation in the higher red-shifted emission for **Di-OMeIm-2TH** arises due to the strong donor behaviour of the $-OCH_3$ groups. This remarkable variation in emission wavelength (λ_{max}) based

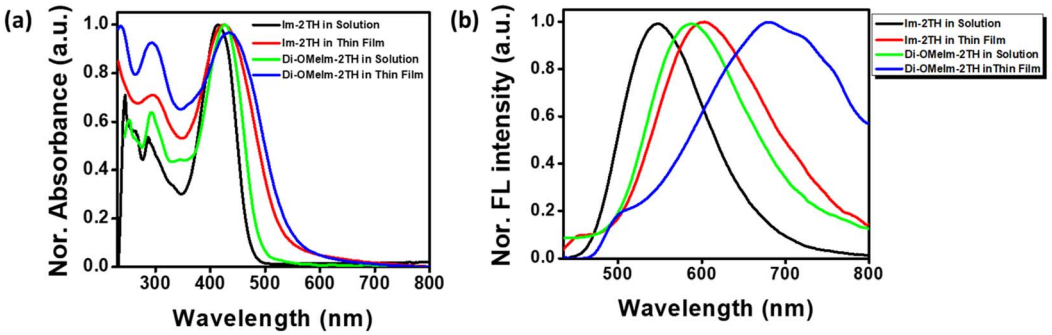

Fig. 1 Absorption (a) and emission (b) spectra of Im-2TH and Di-OMeIm-2TH (10 μM, THF) in solution and thin film.

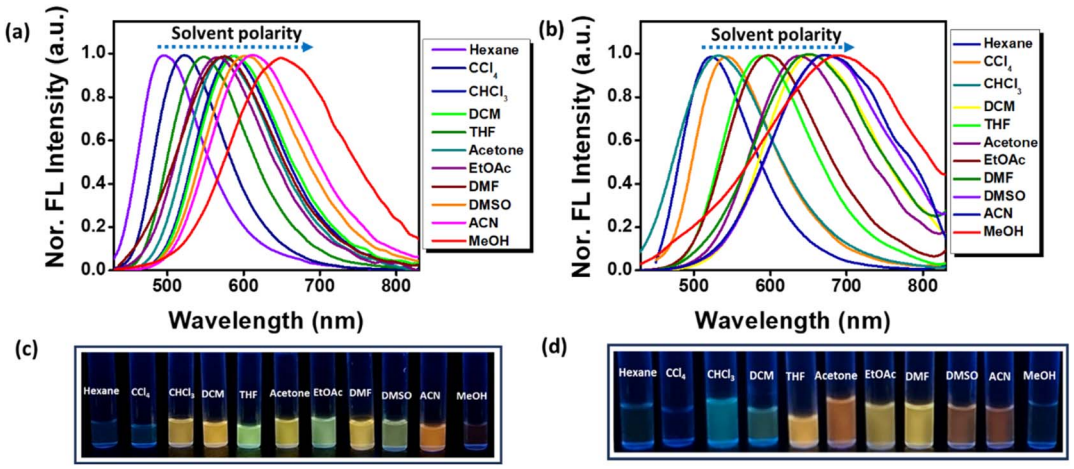

Fig. 2 Normalized emission spectra of (a) Im-2TH and (b) Di-OMeIm-2TH (10 μM) in different solvents. (c and d) Photographs of Im-2TH and Di-OMeIm-2TH dissolved in different solvents under the illumination of a fluorescent light at 365 nm.

on varying solvent polarity confirms the presence of ICT. Fig. 2(c) and (d) show photographs of the variation in the fluorescence colours in different solvents under illumination at 365 nm, respectively. To further validate the charge-transfer process, Lippert–Mataga analysis was performed. The Stokes shift ($\Delta\nu$) varies linearly with the solvent orientation polarizability (Δf) in aprotic solvents. A plot of $\Delta\nu$ *versus* Δf (Fig. S11, SI), the slopes for **Im-2TH** and **Di-OMeIm-2TH** are 14 871 and 18 720, respectively, indicating pronounced solvatochromism and strong ICT character in both compounds. The fluorescence lifetime was calculated in different solvents, which varies with a variation in the solvent polarity. **Im-2TH** shows a lifetime of 1.45 ns in CCl_4, which increases to 1.84 ns in DMSO. Similarly, **Di-OMeIm-2TH** shows a lifetime of 2.56 ns in CCl_4, which decreases to 1.34 ns in DMSO (Fig. S12, SI). The observed blue-shifted emission in DCM and in other polar solvents may attributed to the twisted intramolecular charge transfer (TICT) state, which arises due to the free rotation around the phenyl ring and C=C in the D–A system. The intramolecular rotation converts the local excited states (LE) to TICT, leading to maximum charge separation between the donor and acceptor, stabilized by solvent molecules. To confirm the presence of TICT, we have recorded the emission spectra of **Im-2TH** and **Di-OMeIm-2TH** with varying viscosities with different fractions of ethylene glycol (EG). **Im-2TH** shows an emission band at 678 nm, which appears blue-shifted to 652 nm, and the emission intensity gets enhanced by ~4.8-fold, confirming the presence of TICT in the molecule. In the case of **Di-OMeIm-2TH**, it shows an emission band at ~707 nm in 40% EG, which gets blue-shifted to 678 nm, and the intensity gets enhanced by ~6.5-fold with an increase in viscosity up to 100% EG, confirming the presence of TICT (Fig. S13, SI). To further validate our findings, we measured the quantum yield of **Im-2TH** and **Di-OMeIm-2TH** in various solvents. In non-polar solvents such as

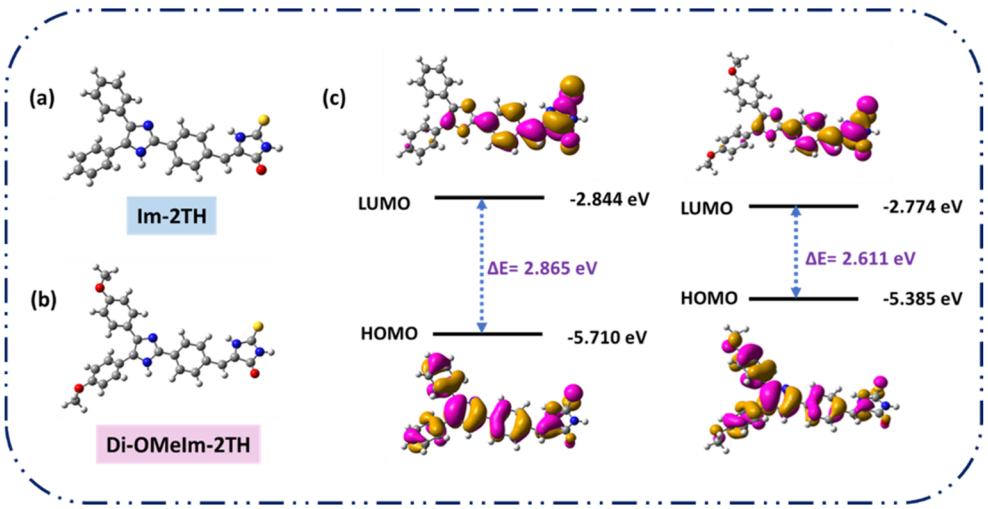

Fig. 3 (a and b) Ground-state optimized structures of Im-2TH and Di-OMeIm-2TH obtained from Gaussian 9.0 using the 6-311G+(d, p) basis set and B3LYP hybrid functional. (c) Frontier molecular orbitals and energy levels of Im-2TH and Di-OMeIm-2TH.

CCl_4, **Im-2TH** shows a quantum yield (Φ) of 25.21%, which significantly increases to 63.42% in pure THF, while decreasing to 3.16% in a highly polar solvent. Similarly, **Di-OMeIm-2TH** shows a quantum yield of 5.17% in CCl_4, which increases to 74% in the case of THF. With a further increase in solvent polarity, the quantum yield starts to decrease, as in the case of DMSO, and **Di-OMeIm-2TH** shows a quantum yield of 21.55%, which further reduces to 1.51% in MeOH. This variation in quantum yield with a variation in the medium polarity confirms the presence of TICT.[32]

To gain more insight on the influence of substitution in electronic and optical properties, computational studies were performed. The energies of the HOMO and LUMO levels of **Im-2TH** and **Di-OMeIm-2TH** in the gas phase were calculated to be −5.71, −5.38, −2.84, and 2.77 eV, respectively. The HOMO–LUMO energy gap of **Im-2TH** and **Di-OMeIm-2TH** was calculated to be ΔE_{H-L} = 2.86 eV and 2.61 eV, respectively. With an increase in the donor strength by introducing the –OMe group into both benzene units, both the frontier molecular orbital (FMO) energy levels increased; however, the HOMO energy level increased considerably more than the LUMO energy level (Fig. 3(a–c)). The smaller the energy band gap, the lower the energy required for an electronic transition, causing the absorption spectrum to shift towards a longer wavelength. The dihedral angle between two phenyl rings in **Im-2TH** is 5.52°, which decreases to 5.39° in **Di-OMeIm-2TH** due to the presence of two methoxy groups on the phenyl ring. Similarly, the dihedral angle between the diphenylimidazole core and the conjugated benzene ring increases from 176.43° to 176.79°, and the dihedral angle between the benzene ring and the 2TH ring increases from 178.87° to 178.91° for **Di-OMeIm-2TH**.

3.1 Trace water detection

Donor–acceptor (D–A)-type organic molecules possess strong ICT behavior. A subtle change in microenvironment can alter CT properties. Water is a dipolar in nature due to the uneven distribution of its electron density. Hence, a small amount of water can alter the CT properties due to its high polarity and ability to form H-bonding. Therefore, we have examined the ability of probes **Im-2TH** and **Di-OMeIm-2TH** to detect trace amounts of water. To demonstrate the potential response behaviour of the probes, we have chosen three different water-miscible polar solvents, such as THF, ACN, and DMSO, which are widely used as solvents in organic reactions, and carried out fluorescence titration experiments. With the gradual addition of water (0–33% v/v) to THF, the fluorescence intensity of **Im-2TH** (10 μM) dramatically decreased by 82% with a red shift of ~94 nm, and the colour changes from green to light orange exhibiting ratiometric behaviour, as shown in Fig. 4(a). Fig. 4(b) describes the change in the quenching behaviour at different volume fractions. At 0–4 v/v%, the quenching efficiency linearly increased, while at 5–33 v/v%, the quenching efficiency increased exponentially by ~2.35 folds, followed by reaching saturation. Further, an increase in the water fractions displayed no significant change in emission quenching. In acetonitrile, **Im-2TH** showed an orange colour emission band at 614 nm, which gets quenched by 85% and is red-shifted to 654 nm with the successive addition of water fractions (0–20% v/v) (Fig. 4(c) and (d)). In DMSO, **Im-2TH** shows a yellow colour emission band at 602 nm, which is quenched by 89%, and subsequently red-shifted to 655 nm with the gradual addition of water (0–33%) (Fig. 4(e) and (f)). The observed red shift in emission

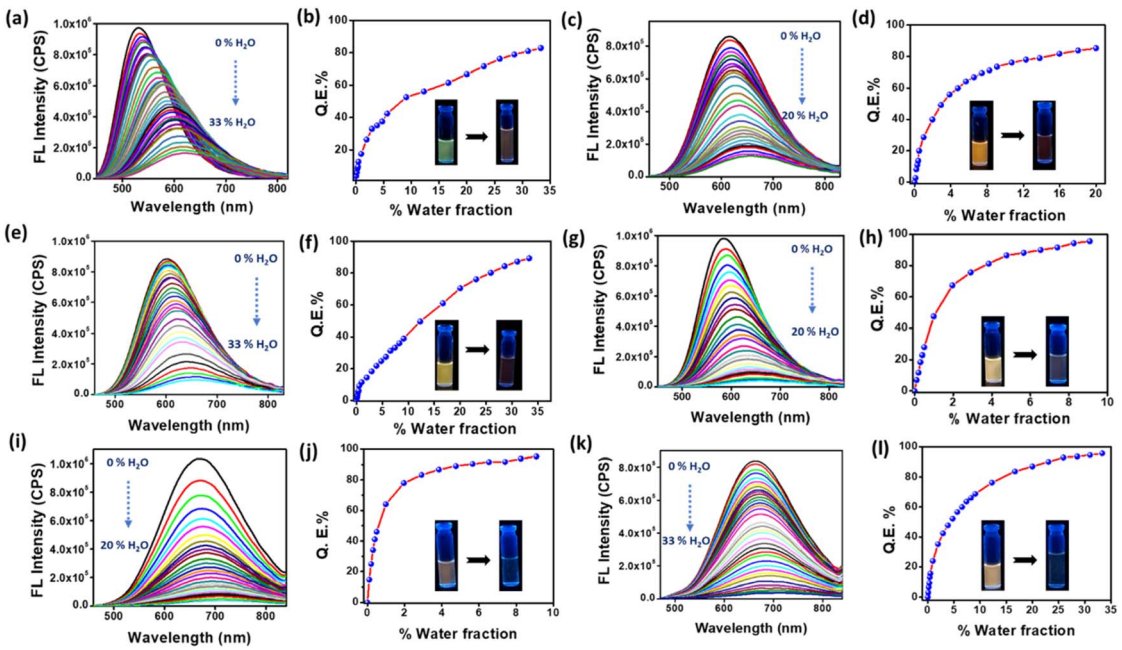

Fig. 4 Changes in the fluorescence emission spectra and quenching efficiency of **Im-2TH** (10 μM) in THF (a and b), ACN (c and d), and DMSO (e and f) with varying water concentrations. Changes in the fluorescence emission spectra and quenching efficiency of **Di-OMeIm-2TH** (10 μM) in THF (g and h), ACN (i and j), and DMSO (k and l) with varying water concentrations. The inset photographs show the variation in the colour under illumination (365 nm).

spectra along with fluorescence quenching can be attributed to polarity effects and intermolecular H-bonding between **Im-2TH** and water molecules.

Similarly, **Di-OMeIm-2TH** in pure THF shows a yellow colour emission band at 585 nm, which gets quenched by 95% and red-shifted to 652 nm with a gradual increase in the water content (0–20% v/v) (Fig. 4(g) and (h)). In acetonitrile, **Di-OMeIm-2TH** shows an orange colour emission band at 670 nm, which gets quenched by 95% and red-shifted to 700 nm with the addition of water (0–20% v/v) (Fig. 4(i) and (j)). In DMSO, a yellow colour emission band appears at 663 nm, which gets quenched by 95% and red-shifted to 700 nm gradually upon the addition of water (0–33%) (Fig. 4(k) and (l)).

Further, we employed the Stern–Volmer (SV) eqn (1) to calculate the quenching association constant (K_{sv}) using eqn (1), as follows:

$$I_o/I = 1 + K_{sv}[Q] \quad (1)$$

where K_{sv} is the quenching constant, [Q] is the quencher concentration, and I_o and I are the fluorescence intensity before and after the addition of water, respectively. The Stern–Volmer plot of I_o/I *vs.* [Q] was plotted to obtain the slope value as K_{sv}. At lower concentrations, I_o/I is found to be linear; however, with an increase in the concentration of water, we observed a slight deviation from linearity with a positive upward curvature. The K_{sv} values of **Im-2TH** were calculated to be 0.4915, 0.8662, and 0.3448 M^{-1} for THF, ACN, and DMSO (Fig. 5(a)–(c)), respectively. Similarly, the K_{sv} values for **Di-OMeIm-2TH** were calculated to be 1.3945, 3.117, and 0.6787 M^{-1} in THF, ACN, and DMSO (Fig. 5(d)–(f)), respectively. Further, fluorescence lifetime measurements were carried out for **Im-2TH** and **Di-OMeIm-2TH** in THF, ACN, and DMSO with different water fractions at their emission maxima using a 450 nm diode laser as the excitation source. Fig. S14, SI illustrates that in all three solvents, the lifetimes of both **Im-2TH** and **Di-OMeIm-2TH** decreases with an increase in water concentration, showing an increase in non-radiative transition with the addition of water. Further, the limit of detection (LOD) was calculated using the formula $3\sigma/m$, where σ is the standard deviation of blank samples and m is the slope of the linear regression curve. **Im-2TH** shows LODs of 0.142 ppm in THF, 0.098 ppm in ACN, and 0.213 ppm in DMSO for trace amounts of water. Similarly, we obtained the LODs for **Di-OMeIm-2TH** as 0.060 ppm in THF, 0.034 ppm in ACN, and 0.124 ppm in DMSO for trace water (Fig. S15, SI).

Table 1 demonstrates that **Di-OMeIm-2TH** is highly sensitive and has a lower detection limit for trace water in comparison to **Im-2TH**. The increased sensitivity of **Di-OMeIm-2TH** to trace water is attributed to the enhanced donor strength of the diphenylimidazole motif, which is caused by the presence of two methoxy groups (–OCH_3). The sensitivity for trace water in different solvents follows the order of ACN > THF > DMSO for both derivatives. Thus, **Im-2TH** and **Di-OMeIm-2TH** display higher sensitivity than previously documented chemosensors for trace water detection in organic solvents (Table S1, SI).

The fabrication of functional nanoscale structures with distinct morphologies *via* energy-efficient and resource-conserving bottom-up approaches *via* self-assembly routes is

Table 1 Summary of the K_{sv} values and LODs of Im-2TH and Di-OMeIm-2TH in different solvents

	Im-2TH		Di-OMeIm-2TH	
Solvent	K_{sv} (M^{-1})	LOD (in ppm)	K_{sv} (M^{-1})	LOD (in ppm)
THF	0.4915	0.142	1.3945	0.060
ACN	0.8662	0.098	3.117	0.034
DMSO	0.3448	0.213	0.6787	0.124

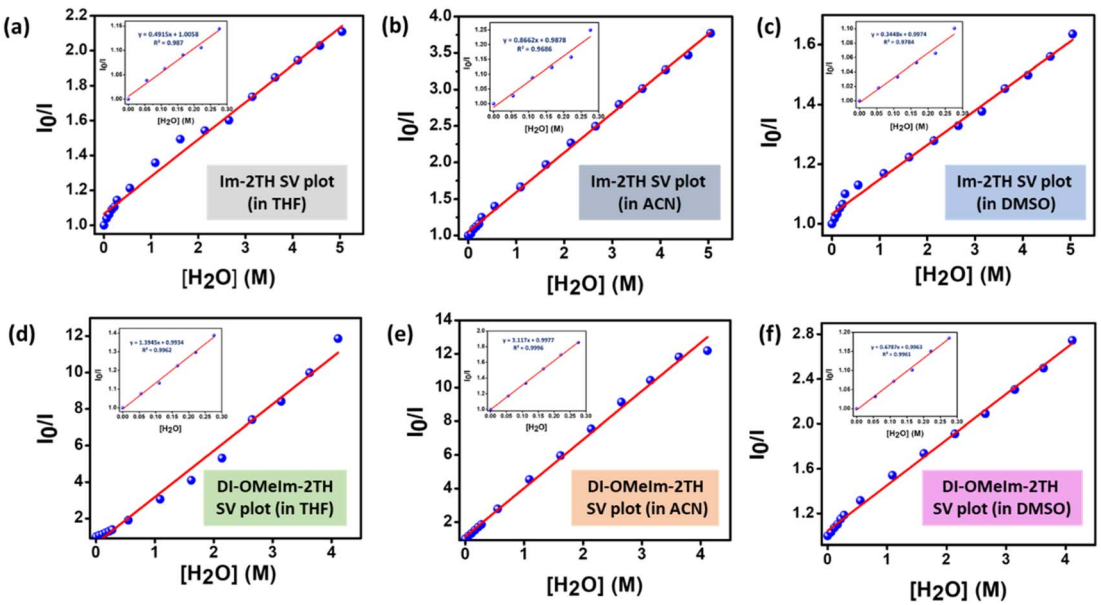

Fig. 5 Stern–Volmer (SV) plots of Im-2TH in different solvents: (a) THF, (b) ACN, and (c) DMSO. SV plots for Di-OMeIm-2TH in different solvents: (d) THF, (e) ACN, and (f) DMSO. Inset graphs show the zoomed view of the SV-plot at a lower concentrations.

an area of interest. The morphology of self-assembled structures plays a crucial role in determining their chemosensing response behaviour. Thus, the fabrication of diverse nanoscale structures from a single molecular entity by varying the self-assembly parameters is extremely important and highly desirable.[33,34] In this context, small π-conjugated molecules are promising building blocks for the development of different nanostructures with various morphologies by fine-tuning external parameters.[35] Therefore, we have examined the aggregation-induced emission (AIE) behaviour of **Im-2TH** and **Di-OMeIm-2TH** by varying the water content in THF. Upon the addition of $f_w = 10\%$ (10% of H_2O and 90% of THF in the case of **Im-2TH**), its emission maximum at 550 nm gets red-shifted to 588 nm with 37% quenching in its emission intensity, and the colour of the probe solution changes from green to orange. With an increase in f_w up to 70%, the emission maximum at 550 nm gets red-shifted to 645 nm with 89% quenching in emission intensity, and the colour of the probe solution changes from dark orange to light orange. This remarkable red shift and quenching of the emission maxima with an increase in water content up to $f_w = 70\%$ indicates the formation of aggregates, which slowly settled down, leading to a decrease in emission intensity. The red-shifted emission band with an increase in f_w up to 70% is primarily due to the stabilization of the lowest unoccupied molecular orbital (LUMO) in the polar medium, which lowers the energy gap associated with that CT transition. Interestingly, at $f_w = 80\%$, the emission maximum at 640 nm gets blue-shifted to 570 nm with an ~1.2-fold enhancement in emission intensity, and the colour of the probe solution changes from light orange to light green.

The dynamic blue-shifted emission maximum with enhanced intensity suggests the formation of different self-assembled aggregates through structural deformation, leading to an aggregation-induced blue-shifted emission ($>f_w = 80\%$) with the formation of H-aggregates. Further, with an increase in the water fraction to $f_w = 90\%$ the emission maximum at 570 nm gets blue shifted to 551 nm with 95% quenching in emission intensity (Fig. S16, SI). Similarly, in the case of **Di-OMeIm-2TH** (10 μM, THF) at $f_w = 10\%$, its emission maximum at 585 nm gets red-shifted to 640 nm, accompanied by 89% quenching in its emission intensity, and the colour of the probe solution changes from orange to colourless. At $f_w = 80\%$, the emission band gets blue-shifted to 605 nm with an ~3.9-folds enhancement in emission intensity, and the solution colour turns into light orange. This clearly demonstrates that at $f_w = 80\%$, **Di-OMeIm-2TH** shows an aggregation-induced blue-shifted emission similar to **Im-2TH**. A further increase in $f_w = 90\%$ led to a blue-shift in the emission maximum from 605 nm to 595 nm with 97% quenching of the emission band (Fig. S17, SI). The AIE behavior of **Im-2TH** and **Di-OMeIm-2TH** at $f_w = 80\%$ can be explained based on restricted intramolecular rotation (RIR) phenomena. Both probes possess free phenyl propellers, which can rotate along the single bond axis, leading to relaxation of the excited state through a non-radiative pathway (up to 70% water-THF). However, in the aggregated state at $f_w = 80\%$, the free rotation is restricted due to surrounding molecules, and relaxation through non-radiative pathways gets impaired.[8,36] The discernible change in fluorescence output with a variation in the water fraction, f_w, in the THF-water ratio originates from the change in the aggregation pattern of the monomeric unit. Therefore, we surmised that **Im-2TH** and **Di-OMeIm-2TH** could self-assemble into distinct morphology in various THF-water mixtures due to the changes in the overall combination of noncovalent interactions. To ascertain this phenomena, we have investigated the morphology of the self-assembled structures formed by **Im-2TH**

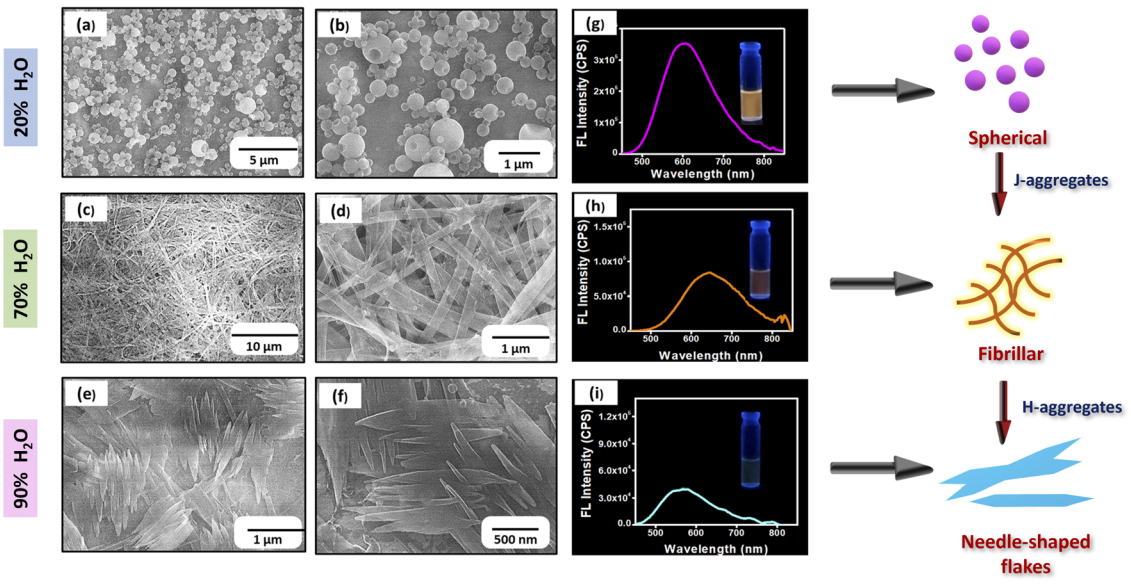

Fig. 6 HR-SEM images of different self-assembled structures formed by **Im-2TH** in different water fractions: (a and b) $f_w = 20\%$, (c and d) $f_w = 70\%$ and (e and f) $f_w = 90\%$. (g–i) Emission spectra of **Im-2TH** at different water fractions, and the inset shows the variation in the fluorescence output of **Im-2TH** under illumination (365 nm).

and **Di-OMeIm-2TH** in THF-water and ACN-water mixtures by varying fractions of water using HR-SEM. At $f_w = 20\%$, **Im-2TH** forms a nanosphere-like superstructure, which transforms to a thin fibrillar-like structure at $f_w = 70\%$. At a higher water percentage of $f_w = 90\%$, **Im-2TH** self-assembled into aggregated needle-shaped nanoflakes (Fig. 6). Similarly, in pure

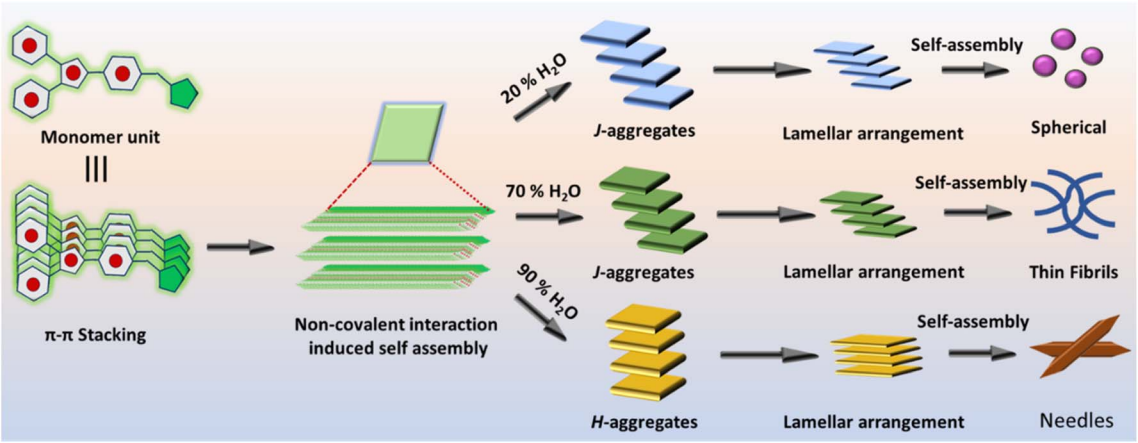

Scheme 2 Pictorial representation of the formation of different self-assembled structures by **Im-2TH** in different THF-water mixtures through a lamellar molecular arrangement, followed by a surface-minimizing self-assembly process.

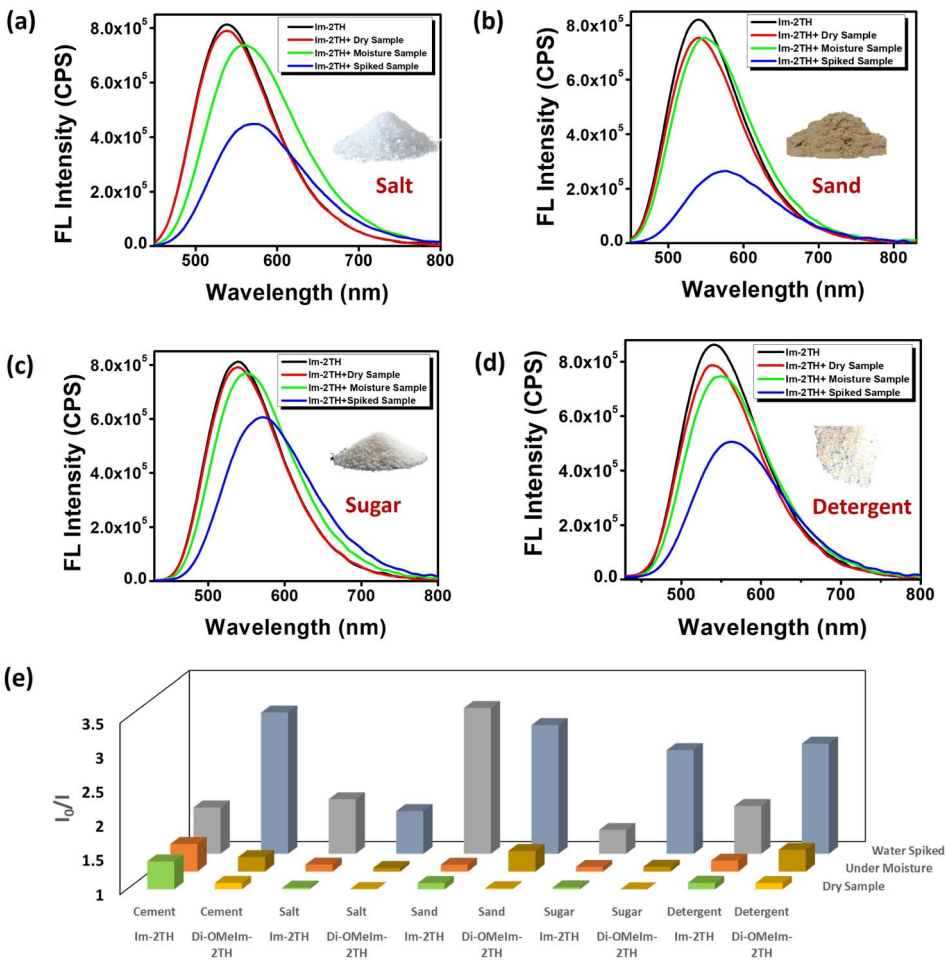

Fig. 7 Changes in the emission intensity of **Im-2TH** (10 μM, THF) in the presence of different commercial products: (a) salt, (b) sand, (c) sugar, and (d) detergent. (e) 3D graph showing the variation in the emission intensity of **Im-2TH** and **Di-OMeIm-2TH** (10 μM, THF) in the presence of different commercial products.

acetonitrile, **Im-2TH** self-assembles into a nanoflake-like structure, which transforms into a branched nanoflake-like structure at f_w = 20% (Fig. S18, SI). Likewise, **Di-OMeIm-2TH** in a 20% water-THF mixture self-assembled into spherical-like structures. Further, with an increase in the water fraction up to 70%, fibrillar aggregates were formed, which transformed into large spherical aggregates at a higher water percentage of f_w = 90%. (Fig. S19, SI). However, in pure acetonitrile, **Di-OMeIm-2TH** shows a nanofiber-like morphology, which transforms into nanosphere-like assemblies with the addition of f_w = 20% (Fig. S20, SI). Scheme 2 shows a pictorial representation of the formation of aggregates under different conditions.

3.2 Detection of trace water in real samples

Moisture is commonly present in food products, and a higher water content promotes humidity, accelerating microbial growth and compromising the stability and freshness of food. Also, in building materials such as cement, moisture can affect their binding efficiency, making the accurate determination of the water content in both raw food and construction materials essential. In this regard, the **Im-2TH** and **Di-OMeIm-2TH** probes were explored for the detection of moisture in raw food materials such as salt, sugar, and detergent powder, as well as in construction materials such as cement and sand, under various conditions, including dry, moist, and wet environments. Fig. 7(a) shows that the emission intensity of **Im-2TH** remains largely unchanged in completely dry salt samples. In samples containing moisture, slight quenching (~0.08%) and a red-shift (~20 nm) are observed. In the spiked salt samples (5% water v/v), the emission intensity decreases by 44% with a red shift of ~29 nm, demonstrating that **Im-2TH** is capable of detecting trace water impurities. In the case of the other spiked samples such as sand, sugar, detergent, and cement, 68.0%, 25.9%, 41.2%, and 40.44% quenching in emission intensity is observed, respectively. Similarly, **Di-OMeIm-2TH** was utilized to detect trace water in real samples. Fig. S21, SI elucidates that in the spiked samples, such as salt, sand, sugar, detergent, and cement, the quenching efficiencies are 38.5%, 65.3%, 60.3%, 61.7%, and 67.3%, respectively, for **Di-OMeIm-2TH**. Motivated by the changes in the fluorescence colour at different fractions of water content in the samples, we strived to study the variation in the colour changes with RGB analysis using a smartphone.

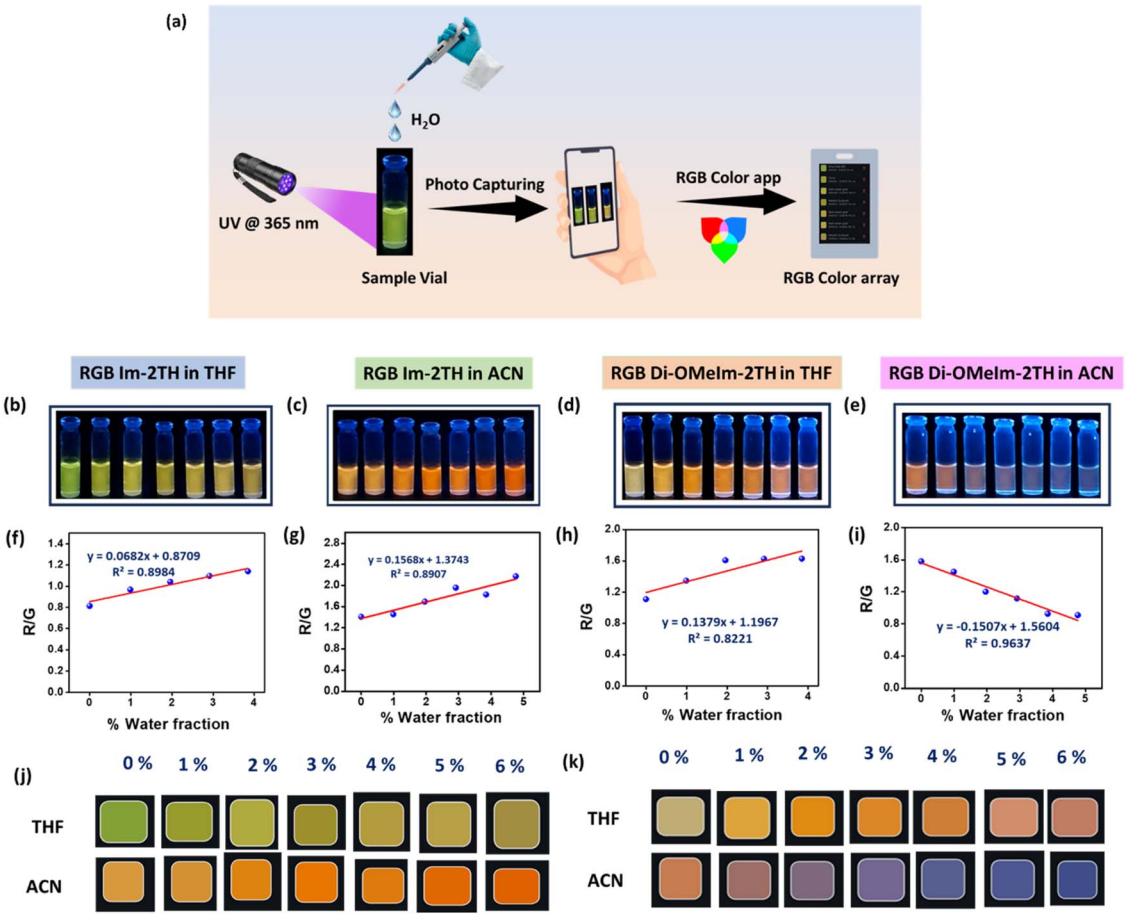

Fig. 8 (a) Schematic of photographing RGB images obtained by the addition of different fractions of water to Im-2TH and Di-OMeIm-2TH using a smartphone. (b–e) Changes in the fluorescence colour of Im-2TH and Di-OMeIm-2TH (10 μM) upon the addition of different water fractions in THF and ACN under illumination (365 nm). (f–i) Variation in the R/G values of Im-2TH and Di-OMeIm-2TH upon the addition of different concentrations of water in THF and ACN. (j and k) Colour array generated from the RGB analysis of Im-2TH and Di-OMeIm-2TH in THF and ACN.

3.3 RGB analysis

Over the past few years, smartphone technology has undergone remarkable advancement. The compact size, portability, user-friendly interface, GPS, and internet connectivity of smartphones provide users with access to high-performance imaging and computing capabilities. In digital images, perceived colour arises from a combination of red (R), green (G), and blue (B) intensities. Each pixel has an RGB value that ranges from 0 to 255. By varying the percentage of R, G, and B, we can produce 16 million distinct colours, for example, the primary colours red (255, 0, 0) and green (0, 255, 0).[37,38] Therefore, RGB analysis is a powerful tool to visualize subtle changes in colour, which is not possible using other techniques. These unique properties motivated us to employ smartphone-assisted RGB profile analysis for detecting the water content in organic solvents in resource-constrained environments.

For this purpose, we added different fractions of water to the organic solvent and simultaneously took a picture under illumination at 365 nm using a smartphone (model SM-A146B/DS) (Fig. 8(b–e)). Further, each digital image was split into its red (R), green (G), and blue (B) components using RGB colour app software, as shown in Fig. 8(f–i). A smartphone-based colour recognition array was developed for the different fractions of water. In pure THF, **Im-2TH** shows an olive drab colour, which transforms to a metallic sunburst colour on adding 0–6% water. In pure acetonitrile and dimethyl sulfoxide, **Im-2TH** shows a satin sheen gold-like colour and copper colour, which converts to Spanish orange and French bistre colour on the addition of 0–6% water (Fig. 8(j) and S22, SI). Similarly, **Di-OMeIm-2TH** in pure THF shows a misty moss colour, which changes to antique brass on adding 0–6% of water. In the case of acetonitrile and dimethyl sulfoxide, the probe alone shows a copper-red colour and French bistre, which change to a purple-navy colour and dark liver (horses) with the addition of 0–6% water, respectively (Fig. 8(k) and S22, SI). Furthermore, portable test strips for water detection were developed using silica-coated thin-layer chromatography (TLC) plates. Probe **Im-2TH** (1 mmol, 10 μL) was coated onto the TLC plates, followed by the addition of varying volumes of water (10–50 μL). The presence of water could be readily detected by the naked eye, accompanied by a visible colour change from light yellow to dark yellow. Under 365 nm UV illumination, the colour changes from brown to dark yellow with an increasing water content. In contrast, **Di-OMeIm-2TH** exhibits negligible fluorescence upon coating and therefore could not be employed for the fabrication of a portable test strip (Fig. S23, SI).

4 Conclusions

In conclusion, two imidazole-based donor–acceptor chromophores, **Im-2TH** and **Di-OMeIm-2TH**, were synthesised *via* the Knoevenagel condensation reaction and characterised by NMR, FTIR, and HR-MS. In both systems, the diphenylimidazole unit functions as a strong electron donor, while the **2-TH** moiety serves as an electron acceptor. In THF, the ICT band undergoes a bathochromic shift with an increase in donor strength, and **Im-2TH** and **Di-OMeIm-2TH** exhibit green and yellow emissions centred at 550 and 585 nm, respectively. Both chromophores display positive solvatochromism, with pronounced bathochromic shifts of ∼120 and 146 nm, respectively. DFT analysis reveals that **Im-2TH** exhibits a larger HOMO–LUMO energy gap (ΔE_{H-L} = 2.86 eV) than **Di-OMeIm-2TH** (ΔE_{H-L} = 2.61 eV), indicating that the introduction of electron-donating groups effectively reduces the band gap and induces a red shift toward longer wavelengths. **Di-OMeIm2TH** shows considerably higher sensitivity with lower detection limits in comparison to **Im-2TH** towards the trace detection of water. The electron-donating –OMe groups present in **Di-OMeIm-2TH** increase its donor behavior, leading to increased CT behaviour. The water-sensing performance of both probes is solvent-dependent, following the order ACN > THF > DMSO. In addition, both chromophores display AIE behaviour and self-assemble into distinct nanoscale morphologies, such as nanospheres and fibrillar structures, upon a variation in the solvent polarity. Importantly, the practical applicability of the probes was demonstrated through the successful detection of trace water in real samples, including raw construction materials (cement and sand), food products (sugar and salt), and commercial detergents. Furthermore, a portable TLC-based test strip and a smartphone-assisted RGB colour recognition assay were developed, enabling the rapid, low-cost, and real-time detection of water impurities in organic solvents. Overall, this work presents a versatile donor–acceptor platform with strong potential for practical moisture sensing in environmental, industrial, and consumer-related applications.

Author contributions

Bhagwat Giri Goswami: conceptualization, methodology, investigation, formal analysis, visualization and writing – original draft. Amutha S: methodology, formal analysis and data curation. Dr Kommineni Kalyani: methodology, formal analysis, data curation and review. Dr K. K. R. Datta: review, editing, formal analysis and supervision. Dr Venkatramaiah Nutalapati: conceptualization, review, editing, funding acquisition and supervision.

Conflicts of interest

The authors declare no competing financial interest.

Data availability

The data supporting this article have been included as part of the supplementary information (SI). Data will be available upon request. Supplementary information: NMR (Fig. S1–S4), FT-IR (Fig. S5), HR-MS (Fig. S6 and S7), optical absorption, steady state fluorescence, fluorescence lifetime decay, AIE, FE-SEM images, and RGB color image array pattern. See DOI: https://doi.org/10.1039/d5ra09696k.

Acknowledgements

NVR greatly acknowledges the Science & Engineering Research Board (SERB), Government of India, for funding through a start-up research grant (SRG/2019/001023) and Central Power Research Institute (CPRI, a government of India society under the Ministry of Power) for funding through the R&D project (CPRI/R&D/TC/GDEC/2022). The authors acknowledge the sophisticated analytical facilities, such as the photo-luminescence spectrometer, NRC, SCIF, and NMR (IIISM) at SRMIST, for enabling analytical characterizations. BG and AS thank SRMIST for the PhD fellowship. BG also acknowledges the Department of Higher Education, Uttarakhand, for giving study leave. NVR also thank SRM University-AP for the seed grant (SRMAP/URG/SEED/2025-26/100).

Notes and references

1 S. Pawar, U. K. Togiti, A. Bhattacharya and A. Nag, Functionalized Chitosan–Carbon Dots: A Fluorescent Probe for Detecting Trace Amount of Water in Organic Solvents, *ACS Omega*, 2019, **4**, 11301–11311.

2 H. S. Jung, P. Verwilst, W. Y. Kim and J. S. Kim, Fluorescent and colourimetric sensors for the detection of humidity or water content, *Chem. Soc. Rev.*, 2016, **45**, 1242–1256.

3 D. B. G. Williams and M. Lawton, Drying of Organic Solvents: Quantitative Evaluation of the Efficiency of Several Desiccants, *J. Org. Chem.*, 2010, **75**(24), 8351–8354.

4 J. Kay, R. Thomas, J. Gruenhagen and C. J. Venkatramani, Simultaneous quantitation of water and residual solvents in pharmaceuticals by rapid headspace gas chromatography with thermal conductivity detection (GC-TCD), *J. Pharm. Biomed. Anal.*, 2021, **194**, 113796.

5 P. Kumar, A. Ghosh and D. A. Jose, Chemical Sensors for Water Detection in Organic Solvents and their Applications, *ChemistrySelect*, 2021, **6**(4), 820–842.

6 P. Kumar, R. Kaushik, A. Ghosh and A. D. Jose, Detection of Moisture by Fluorescent OFF-ON Sensor in Organic Solvents and Raw Food Products, *Anal. Chem.*, 2016, **88**, 11314–11318.

7 S. I. Ohira, K. Goto, K. Toda and P. K. Dasgupta, A Capacitance Sensor for Water: Trace Moisture Measurement in Gases and Organic Solvents, *Anal. Chem.*, 2012, **84**, 8891–8897.

8 M. M. Zafar, R. Yadav, A. Singh, N. Tyagi, A. Samanta and R. K. Mishra, Tetrasubstituted imidazole-based multifunctional fluorophores: trace water detection and lipid droplet (LD) imaging studies, *Chem. Commun.*, 2025, **61**, 9091–9094.

9 Y. Sun, X. Liang, S. Wei, J. Fan and X. Yang, Fluorescent turn-on detection and assay of water based on 4-(2-dimethylaminoethyloxy)-*N*-octadecyl-1,8-naphthalimide with aggregation-induced emission enhancement, *Spectrochim. Acta, Part A*, 2012, **97**, 352–358.

10 L. Ding, Z. Zhang, X. Li and J. Su, Highly sensitive determination of low-level water content in organic solvents using novel solvatochromic dyes based on thioxanthone, *Chem. Commun.*, 2013, **49**, 7319–7321.

11 J. S. Kim, M. G. Choi, Y. Huh, M. H. Kim, S. H. Kim, Y. Wang and S.-K. Chang, Determination of Water Content in Aprotic Organic Solvents Using 8-Hydroxyquinoline Based Fluorescent Probe, *Bull. Korean Chem. Soc.*, 2006, **27**, 2058.

12 Y. C. Liu, G. D. Lu, J. H. Zhou, J. W. Rong, H. Y. Liu and H. Y. Wang, Fluoranthene dyes for the detection of water content in methanol, *RSC Adv.*, 2022, **12**, 7405–7412.

13 M. Basak and G. Das, Amine-incorporated quinoxaline based fluorescent sensor for detection of trace water: Solvent influenced self-assembly, *Spectrochim. Acta, Part A*, 2022, **280**, 121521.

14 X. M. Song, Z. C. Feng, Y. Wu, J. L. Song, L. F. Wei and S. Y. Zeng, Triphenylamine-based conjugated fluorescent sensor for highly sensitive detection of water in organic solvents, *J. Mol. Liq.*, 2022, **365**, 120086.

15 N. Li, X. Dong, X. Lv, Y. Li, Q. Ma, R. Guan and Z. Xie, Liquid and solid-state tunable fluorescent carbon dots for trace water detection, *Chem. Commun.*, 2023, **59**, 4475–4478.

16 J. Tagare, R. Boddula, R. A. K. Yadav, D. K. Dubey, J. H. Jou, S. Patel and S. Vaidyanathan, Novel imidazole-alkyl spacer-carbazole based fluorophores for deep-blue organic light emitting diodes: Experimental and theoretical investigation, *Dyes Pigm.*, 2021, **185**, 108853.

17 J. Tagare, D. K. Dubey, R. A. K. Yadav, J. H. Jou and S. Vaidyanathan, Triphenylamine-imidazole-based luminophores for deep-blue organic light-emitting diodes: experimental and theoretical investigations, *Mater. Adv.*, 2020, **1**, 666–679.

18 B. P. Debata, M. D. Thiyagarajan, R. Prathap, J. D. Girase, S. K. Iyer, S. Patel and S. Vaidyanathan, Benzil-imidazole blue fluorophores and their applications in blue/white light-emitting diodes, sensing and anticounterfeiting, *J. Mater. Chem. C*, 2024, **13**, 2711–2731.

19 P. K. Megha and K. Singh, Imidazole-based probe for the "light-up" detection of hypochlorite ion based on protonation-deprotonation strategy: Applications in real samples, *Dyes Pigm.*, 2024, **228**, 112249.

20 U. Krishnan and S. Kulathu Iyer, Iminothiophenol Schiff base-based fluorescent probe for dual detection of Hg^{2+} and Cr^{3+} ions and its application in real sample analysis, *J. Photochem. Photobiol., A*, 2022, **425**, 113663.

21 X. Yu, Y. Li, Y. Li, Y. Liu and Y. Wang, A highly sensitive fluorescent sensor for reversible visual detection of fluoride ion and trace water in food products, *Spectrochim. Acta, Part A*, 2025, **326**, 125245.

22 M. K. Ravindra, G. P. Darshan, D. R. Lavanya, K. M. Mahadevan, H. B. Premkumar, S. C. Sharma, H. Adarsha and H. Nagabhushana, Aggregation induced emission based active conjugated imidazole luminogens for visualization of latent fingerprints and multiple anticounterfeiting applications, *Sci. Rep.*, 2021, **11**, 16748.

23 P. P. Gawas, B. Ramakrishna, N. Veeraiah and V. Nutalapati, Multifunctional hydantoins: recent advances in optoelectronics and medicinal drugs from Academia to the chemical industry, *J. Mater. Chem. C*, 2021, **9**, 16341–16377.

24 P. P. Gawas, B. Ramakrishna, R. Pamanji, J. Selvin and V. Nutalapati, A novel triphenylamine based push–pull

fluorophore bearing a 2-thiohydantoin unit for toxic Hg^{2+} ion detection: exploring its potential for live cell imaging, *Mater. Adv.*, 2023, **5**, 336–348.

25 P. P. Gawas, K. Selvaraj, R. Pamanji, J. Selvin and V. Nutalapati, Highly sensitive fluorescence turn-OFF and reversible chemical sensor for Hg^{2+} ion based on pyrene appended 2-thiohydantoin, *Chemosphere*, 2024, **352**, 141470.

26 P. P. Gawas, A. Bora, R. P. Reji, B. Ramakrishna, P. B. Managutti, C. R. Göb, S. Mohamed, Y. Kawazoe, S. Velappa Jayaraman, Y. Sivalingam and V. Nutalapati, Substituent Effect on Stimuli-Responsive Donor–Acceptor Framework-Based 2-ThiohydantoinsforMonitoringNonanalVapors, *J. Phys. Chem. C*, 2023, **127**, 6466–6482.

27 K. Selvaraj, P. Palanisamy, B. Ramakrishna, R. Pamanji, J. Selvin, K. Srikanth, S. Nasiri, S. Kment and V. Nutalapati, Fluoranthene-terminated terpyridine ensemble for fluorescence light up and ratiometric chemical sensor for multi toxic metals, *Anal. Chim. Acta*, 2023, **1274**, 341526.

28 P. Palanisamy, M. Anandan, G. Raman and V. Nutalapati, Antenna effect on Zn(II) porphyrin–based molecular ensembles for the detection of 2,4-dinitrophenol through energy and electron transfer process, *Microchim. Acta*, 2025, **192**, 1.

29 P. Palanisamy, M. Anandan, H. K. Vikraman, G. Raman, S. R. N. K. Mangalampalli and V. Nutalapati, Orthogonal and antenna effects on the chemosensing behaviour of porphyrins towards 2,4,6-trinitrophenol: Colour recognition and portable photodiode device, *J. Lumin.*, 2025, **277**, 120988.

30 B. G. Goswami, A. Selvaganesan, K. K. R. Datta and V. Nutalapati, Phenanthroimidazole-based fluorescent nanofibers with 2-thiohydantoin for mercury detection and plant tissue bioimaging, *Food Chem.*, 2026, **499**, 147286.

31 U. Krishnan, S. Manickam and S. Kulathu Iyer, Turn-off fluorescence of imidazole-based sensor probe for mercury ions, *Sens. Diagn.*, 2023, **3**, 87–94.

32 J. Zhang, B. He, Y. Hu, P. Alam, H. Zhang, J. W. Y. Lam and B. Z. Tang, Stimuli-Responsive AIEgens, *Adv. Mater.*, 2021, **33**(32), e2008071.

33 A. Maity, A. Dey, M. Gangopadhyay and A. Das, Water induced morphological transformation of a poly(aryl ether) dendron amphiphile: helical fibers to nanorods, as light-harvesting antenna systems, *Nanoscale*, 2018, **10**, 1464–1473.

34 A. T. Haedler, K. Kreger, A. Issac, B. Wittmann, M. Kivala, N. Hammer, J. Köhler, H. W. Schmidt and R. Hildner, Long-range energy transport in single supramolecular nanofibres at room temperature, *Nature*, 2015, **523**, 196–199.

35 S. Singh, P. K. Hansda, S. Das, M. Douzapau and D. Haldar, In Vitro and In Live-Cell Rapid Hydrazine Detection by Disaggregation of the AIEgen Microstructure, *Chem.–Asian J.*, 2025, **20**, e00399.

36 Y. Hong, J. W. Y. Lam and B. Z. Tang, Aggregation-induced emission: phenomenon, mechanism and applications, *Chem. Commun.*, 2009, 4332–4353.

37 Pratibha, A. Kapoor, J. K. Rajput and A. Kumar, Dualistic Fluorescence as Well as Portable Smartphone-Assisted RGB-Relied Sensing Assay for the Ultra-Sensitive Determination of Pendimethalin in Food and Water Samples by AIEE Active Organic Probes, *Anal. Chem.*, 2022, **94**, 17685–17691.

38 T. T. Wang, C. kit Lio, H. Huang, R. Y. Wang, H. Zhou, P. Luo and L. Sen Qing, A feasible image-based colourimetric assay using a smartphone RGB camera for point-of-care monitoring of diabetes, *Talanta*, 2020, **206**, 120211.